Heterogeneous Metasurface for High Temperature Selective Emission

D. Woolf[1,a)], J. Hensley[1],

[1]*Physical Sciences Inc., 20 New England Business Center, Andover, Massachusetts, 01810, USA*

J. G. Cederberg[2], D. Bethke[2], A. Grine[2], and E. A. Shaner[2]

[2]*Sandia National Laboratories, P.O. Box 5800, Albuquerque, New Mexico, 87185, USA*

We demonstrate selective emission from a heterogeneous metasurface that can survive repeated temperature cycling at 1300 K. Simulations, fabrication and characterization were performed for a cross-over-a-backplane metasurface consisting of platinum and alumina layers on a sapphire substrate. The structure was stabilized for high temperature operation by an encapsulating alumina layer. The geometry was optimized for integration into a thermophotovoltaic (TPV) system and was designed to have its emissivity matched to the external quantum efficiency spectrum of 0.6 eV InGaAs TPV material. We present spectral measurements of the metasurface that result in a predicted 22% optical-to-electrical power conversion efficiency in a simplified model. Furthermore, this broadly adaptable selective emitter design can be easily integrated into full-scale TPV systems.

Thermophotovoltaic (TPV) energy conversion was first identified as a promising technology for converting waste heat into electricity in the 1960s[1]. Since then, work has demonstrated the potential of combustion-TPV systems to act as compact, portable power sources with energy densities nearly 10 times that of rechargeable batteries[2,3] that are critical for a broad range of military and commercial applications. TPV systems convert thermal radiation emitted from a high temperature source (the emitter) into electricity by means of a photovoltaic (PV) diode. If we treat a TPV system as a heat engine with hot (T_{BB}) and cold side (T_{PV}), we can calculate the theoretical thermodynamic (Carnot) efficiency limit: $\eta_{Carnot} = [T_{BB}-T_{PV}]/T_{BB}$. For T_{BB} = 1300 K and T_{PV} = 300 K, η_{Carnot} = 0.77. In practice, the efficiencies of TPV systems have been fundamentally limited to ~15% by the mismatch between the blackbody spectrum of the heated emitter and the external quantum efficiency (EQE) of the TPV material. (Other system considerations have reduced demonstrated efficiencies of combustion-TPV systems to ~2.5%.[3]) Thus, a significant amount of work over the past 30 years has focused on improving the optical-to-electrical conversion efficiency by recycling out of band photons[4], using multiple bandgap cells[5], modifying the emissivity of an object away from the typical blackbody[6–8], or a combination of these techniques[9].

Numerous geometries for modifying the emission spectrum have been studied, including metal (such as tungsten) photonic crystals[7,10], inverse opals[11], and metal-dielectric-metal (MDM) metasurfaces[8,12-14]. While the first

a Author to whom correspondence should be addressed. Electronic mail: dwoolf@psicorp.com.

two groups have shown promise regarding emissivity and survivability at operating temperatures, questions remain about the ability to scale these geometries beyond laboratory demonstrations. MDM metasurfaces, on the other hand, can easily be fabricated by standard foundry lithography techniques while exhibiting extremely tailorable emission spectra that can be made angle-independent when the layer thicknesses are significantly sub-wavelength.[8] The main limitation of the MDM metasurface geometry has been the presence of interfacial stress in the multilayer stack that can lead to delamination at high temperature. However, this issue can be mitigated by properly choosing non-reactive metals and dielectrics that have matching coefficients of thermal expansion (CTEs) from room temperature to > 1300 K. In this letter, we report on the modeling, fabrication, and characterization of a MDM metasurface with a dielectrically symmetric geometry comprised of a platinum (Pt) cross above a Pt backplane, an alumina (Al_2O_3) spacer layer and Al_2O_3 encapsulation on a sapphire substrate that survived repeated temperature cycling to 1300 K. With this geometry, our model predicts at least 23% photonic-to-electronic energy conversion efficiency, 43% spectral efficiency, and 1.2 W/cm^2 of output power when coupled with a 0.6 eV strain-relaxed InGaAs PV cell[15].

Our emitter design is shown in Figure 1(a). The design has five degrees of freedom: p (unit cell period), h (thickness of the spacer layer), t (thickness of the cross), w (long dimension of the cross), and l (short dimension of the cross). We use Pt as our metal because it has good optical properties and should not oxidize at temperatures below 1500 K in an air environment. Additionally, it has well matched CTE to Al_2O_3 from room temperature to 1500 K[16], decreasing the likelihood of delamination of a Pt/ Al_2O_3 stack. The geometry is similar to that used in previous demonstrations[12,14,17], though our final design uses an encapsulation layer and operates in a different design parameter regime. The mechanism for the resonance has been previously described[18].

The fabrication procedure is outlined in Figure 1(b). To begin, an optically thick (200 nm) layer of Pt (with a 20 nm chrome adhesion layer) and $h = 90$ nm thick layer of Al_2O_3 were e-beam evaporated onto a crystalline sapphire (Al_2O_3) wafer (MTI Corp). Next a layer of ZEP-520 e-beam resist (EBR) was spun onto the wafer, exposed by an e-beam writer, and then developed to expose the Al_2O_3 underneath. A second layer of Pt (thickness $t = 45$ nm) was then deposited on the whole chip, followed by lift-off of the EBR. An SEM image of a device array at this stage in the fabrication process can be seen in the inset of Figure 2(a). Finally, an additional 150 nm-thick layer of Al_2O_3 was deposited via Atomic Layer Deposition (ALD) to encapsulate the crosses (Figure 2(b), inset). We fabricated twenty five 500 $\mu m \times 500\ \mu m$ arrays of crosses, with 400 nm < p < 600 nm, 150 nm < l < 250 nm, 250 nm < w < 300 nm in

each emitter array. (Note that $w=l$ corresponds to a square.) We chose these numbers based on reflectance simulations of the unencapsulated structure performed using the FDTD (finite difference time domain) Solutions package from Lumerical Solutions, Inc. A search of parameter space led to a set of optimized parameters that resulted in a broad and deep reflection dip that is independent of the incident angle of radiation. A representative reflectivity spectrum can be seen in Figure 2(a) (green line), for w = 275 nm, l = 150 nm, p = 400 nm, h = 90 nm, and t = 45 nm.

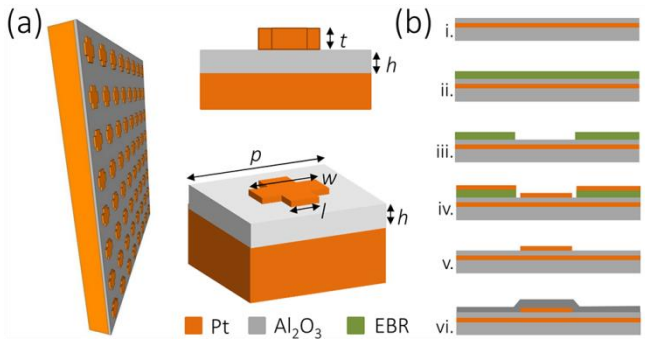

FIG. 1. (a) Metasurface design consisting of an array of platinum crosses above a platinum backplane with an amorphous Al_2O_3 spacer layer. (A final Al_2O_3 encapsulation layer on top of the Pt crosses is left out of the image for clarity.) A perspective (top center) and birds-eye view (bottom center) of a unit cell of the metasurface are labeled with the five device design parameters: t, h, p, w, and l. The encapsulation thickness is 150 nm. (b) Fabrication procedure. i. Pt and Al_2O_3 are e-beam evaporated. ii. E-beam resist (EBR) is spun. iii. Cross pattern is written in resist via e-beam writer and is developed. iv. Pt is evaporated. v. Resist is removed. vi. Al_2O_3 is deposited using Atomic Layer Deposition.

We measured the unencapsulated (blue line, Figure 2(a)) and encapsulated (Figure 2(b)) structures in a microscope-coupled Fourier-transform infra-red (FTIR) spectrometer fitted with a HgCdTe detector. By comparing the curves in Figure 2(a), we can see good agreement between simulation and experiment. FTIR measurements of the encapsulated sample's infra-red absorption features (Figure 2(b)) reveal a broadening of the resonances compared to the unencapsulated structure.

To test the multilayer structure's robustness to high-temperature thermal cycling, we annealed the encapsulated samples in an argon atmosphere at 1300 K, in two, five and five minute increments. After each annealing cycle, we characterized the emitter arrays with the FTIR spectrometer through an optical microscope. Two measurements with were taken with the FTIR to measure the reflectivity between 0.9 and 3.2 μm and between 3.2 and 10 μm, respectively. Figure 3(a) shows the FTIR spectrum for a particular pattern (w = 275 nm, l = 250 nm, p = 550 nm) before thermal cycling (red), after the first two-minute cycle (green) and after three cycles and twelve total minutes at 1300 K (blue). The slight shift from the pre-baked spectrum after the first bake is likely due to a measured 5 nm change in the thickness of the ALD-deposited Al_2O_3 that occurred because of densification during the initial anneal. Figure 3(b) and (c) show an optical image for 10 of the 25 pre-anneal encapsulated metamaterial arrays and a

representative SEM image of four unit cells of one of the arrays, respectively. Figure 3(d) and (e) are the same as (b) and (c) but after the three thermal cycles. By comparing the pre- and post-cycle images we notice no discernable macroscopic change in the visible-frequency spectral properties or microscopic change in the shape of the encapsulated crosses after all three thermal cycles. Additionally, there is no evidence of delamination anywhere on the chip, as the post-anneal sample resembles the pre-anneal sample. Combined with the FTIR measurements, these results indicate that the encapsulated structure is highly stable to thermal cycling.

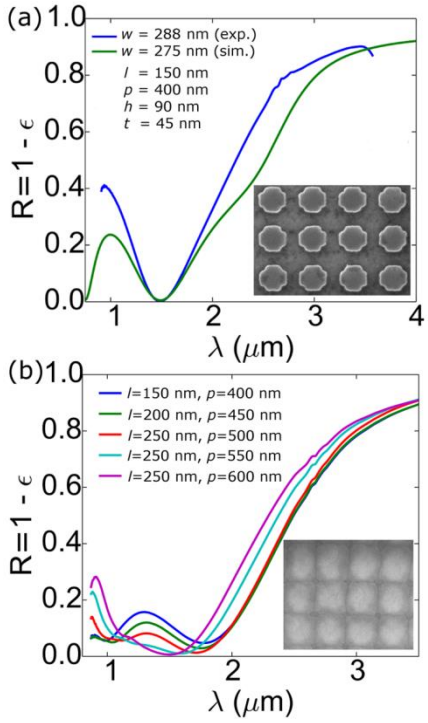

FIG. 2. (a): Comparison of simulated and experimental reflectance spectra for the unencapsulated structure. (b) Variation in reflectance spectra five different encapsulated structures with w = 275 nm. SEM images of the unencapsulated (a) and encapsulated (b) structures are shown in the insets. The SEM image of the encapsulated structure appears blurry because the imaging electrons do not penetrate the encapsulating layer.

For comparison, we plot the same data for the unencapsulated structure (Fig. 3(f)-(j)). Upon heating, the Pt crosses undergo a morphological change (Fig. 3(j) inset compared to Fig. 3(h)) to lower their energy by reducing their surface area, forming globules, which results in a dramatic shift in the infrared reflection spectra (Fig. 3(d), red to green line) as well as the optical appearance (Fig. 3(g) to (i)). The morphological change occurs within the first two minutes at 1300 K and the new surface configuration is stable to additional heating and temperature cycling, as indicated by the similarity between the blue and green curves. Recent work[14] demonstrated robust operation up to 900 K of a Pt/Al_2O_3 metasurface but without the encapsulation layer. Our results indicate that the encapsulation layer is necessary to reach temperatures > 1300 K for integration into efficient TPV systems.

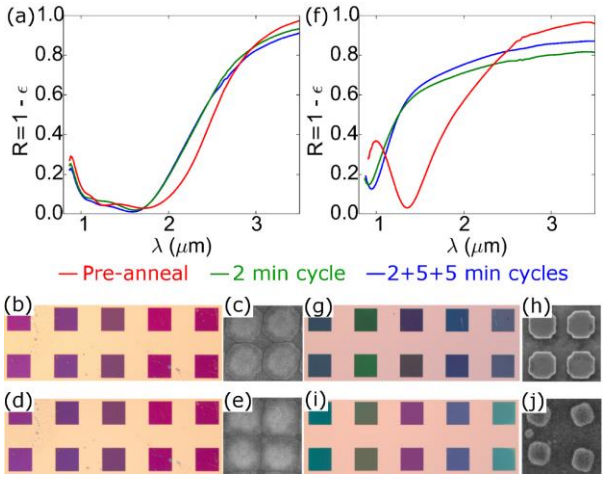

FIG. 3. (a) Reflectivity of the encapsulated emitter before (red), after a two minute thermal anneal cycle at 1300 K (green) and after three cycles and 12 total minutes at 1300 K (blue). (b) Pre-anneal optical image of ten of the 500um x 500um arrays. (c) SEM image of one part of one of the arrays. (d,e): Post-anneal optical and SEM images revealing no microscopic or macroscopic morphological change in the metasurface. (f-j): Same as (a-e) but for the unencapsulated structure. The change in the reflectivity after annealing is reflected in the visible frequency spectrum optical image (i) and the SEM image (j) showing a morphological change. All curves in (a) and (f) correspond to the emitter array in the second row and fourth column of the optical images, with w = 275 nm, l = 250 nm, p = 550 nm.

We used the measured, room temperature absorption spectra to represent the emissivity ($\varepsilon_{emit}(\omega) = 1 - R(\omega)$) of the metasurface at high temperature. While other metals, such as tungsten[19], have shown their emissivity above 2μm increase >30% at 1300 K compared to room temperature (as predicted by a temperature-dependent Drude model[20]), two recent publications[14,21] indicated no quantifiable change in the emissivity of platinum, though further studies are needed to properly quantify the emissivity of Pt as a function of temperature. We thus use the room-temperature emissivity to model how well our emitter will behave in a TPV system (Figure 4) and calculate the TPV cell efficiency η_{TPV} and the generated power P_{out}. We can understand η_{TPV} as the product of the power-spectral efficiency (η_{ps}: power absorbed by the PV diode divided by the power emitted by the selective emitter, P_{rad}) and the diode's efficiency (η_{diode}: power conversion efficiency of absorbed photons). Consequently, we can write

$$\eta_{\mathrm{TPV}} = \eta_{\mathrm{ps}}\eta_{\mathrm{diode}} = \frac{P_{abs}}{P_{rad}}\frac{P_{out}}{P_{abs}} = \frac{V_{OC}I_{SC}FF}{P_{rad}} \quad (1)$$

where V_{OC} is the diode's open circuit voltage, I_{SC} is the diode's short circuit current, and FF is the fill factor, which will be defined below. Since the emitter is at T_{emit}=1300 K and the PV diode is at T_{PV} = 300 K, the amount of power radiated to the TPV cell from the emitter can be expressed as:

$$P_{rad} = \int_0^\infty \frac{\omega^2}{(2\pi)^2 c^2} \frac{\hbar\omega}{\exp\left(\frac{\hbar\omega}{kT_{emit}}\right) - 1} \varepsilon(\omega) d\omega, \tag{2}$$

where c is the speed of light, k is the Boltzmann constant, $\hbar$ is the reduced Planck constant, ω is the angular frequency, and we are ignoring the negligible radiation path from the PV cell to the emitter because $T_{emit} >> T_{PV}$ and we are assuming angle and polarization-independent emission and an anti-reflection (AR) coated PV cell. The integrand of Eq. 2 with $\varepsilon = 1$, assuming a perfect blackbody, is drawn as the green dashed line in Fig. 4 and plotted on the right vertical axis, while the emissivity ε_{emit} (blue line) is plotted along the left vertical axis. The full integrand of Eq. 2 (the product of the blackbody power spectrum and ε_{emit}) represents the actual radiated power spectrum at 1300 K and is plotted as the cyan line along the right vertical axis.

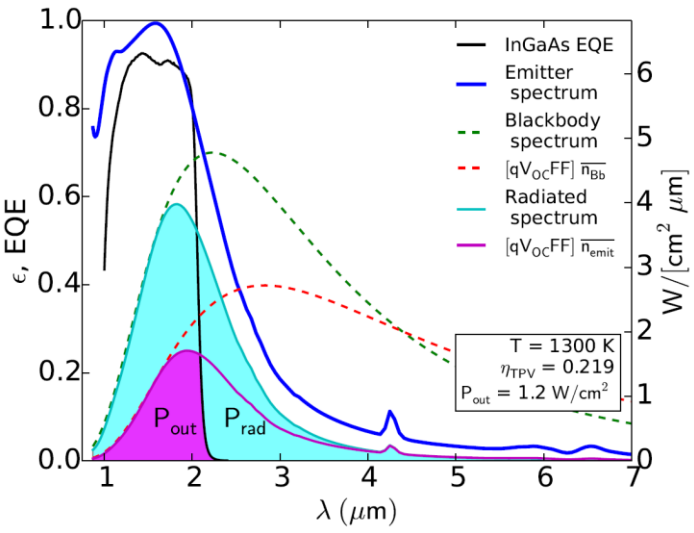

FIG. 4. Model of selective emitter-TPV system at 1300 K. The black body power (dashed-green line) and normalized photon density (dashed red line) spectra are plotted on the right vertical axis and used to calculate the radiated power (cyan line) and radiated photon density (magenta line) of the selective emitter, respectively (also plotted on the right vertical axis). The emissivity, ε, of the metasurface (blue line) and the EQE of the PV material (black line) are plotted along the left vertical axis. The shaded cyan and magenta volumes represent the radiated power at the emitter (P_{rad}) and the power absorbed by the PV material (P_{out}), respectively. The feature at 4.25 μm is an artifact of the measurement setup.

The amount of power generated by the PV cell (P_{out}) is proportional to the number of electron-hole pairs generated and thus is also proportional to the number of emitted, above-bandgap *photons*, n_{emit} (as opposed to the emitted *power* density) which we can write as

$$n_{emit} = \int_{\omega_g}^\infty \frac{\omega^2}{(2\pi)^2 c^2} \frac{1}{\exp\left(\frac{\hbar\omega}{kT_{emit}}\right) - 1} \varepsilon(\omega) d\omega \,. \tag{3}$$

The EQE of the TPV material is defined as the percentage of incident photons converted to electron-hole pairs and is plotted as the black line against the left vertical axis of Fig. 4. The integrand of Eq. 3 with $\varepsilon = 1$ represents a blackbody photon density ($\overline{n_{BB}}$) at 1300 K and is plotted as the red dashed line. The integrand with $\varepsilon = \varepsilon_{emit}$ represents the emitted photon density of our metamaterial emitter, $\overline{n_{emit}}$, and is plotted as the magenta line. Both curves are normalized by $qV_{OC}FF$ to place them in units of power so that they can be plotted along the right vertical axis. To obtain this normalization, we use the standard model of a PV diode[22] with the dark current set to the thermodynamic limit[23] ($I_{dark} = q(n^2+1)E_g^2 k_B T_{pv}/(4\pi^2\hbar^3c^2)\exp(-E_g/k_B T_{pv}) = 0.18\ \mu A/cm^2$) to find I_{SC} and V_{OC} and then find the maximum extractable power by finding V_{max} and I_{max}, which allows us to calculate the maximum fill factor $FF = I_{max}V_{max}/I_{SC}V_{OC} =$ 0.745, which agrees well with reported data for our material[24]. Using this normalization, we can visually observe in Figure 4 the relevant figures of merit for our selective emitter. The shaded cyan and magenta areas correspond to P_{rad} and P_{out}, respectively, and thus η_{TPV} is visually approximated by the ratio of the magenta area to the cyan area. Additionally, the spectral efficiency (η_{spec}) – the percentage of emitted photons converted to electron-hole pairs – is the ratio of the shaded magenta area to the full area under the magenta curve.

We characterized the post-thermal cycling emissivity of all twenty five arrays and found that the highest efficiency-power product $\eta_{TPV}P_{out}$ corresponded to w = 288 nm, l = 250 nm, p = 600 nm when paired with the 0.6 eV InGaAs TPV material, generating 1.2 W/cm^2 with $\eta_{TPV} = 0.22$ and $\eta_{spec} = 0.43$. For comparison, replacing our selective emitter with a perfect black body emitter results in 1.3 W/cm^2 with $\eta_{TPV} = 0.08$ and $\eta_{spec} = 0.10$. Our selective emitter succeeds by significantly suppressing the emission of below-bandgap photons and having the peak of the emissivity align with the peak of the TPV EQE. The poor performance of a TPV system without a selective emitter can be seen in Fig. 4 by looking at the areas under the dashed green and red curves. The vast majority of emitted photons (90%) are below-bandgap, corresponding to energy that will not be converted to electricity and that could be absorbed elsewhere in the PV structure, which could raise the temperature of the TPV material and decrease its EQE. The selective emitter improves the efficiency of an overall combustion-TPV system by increasing η_{TPV}, thus decreasing wasted emission and also the amount of fuel needed to keep the emitter at 1300 K.

Additional gains in efficiency and output power could be achieved by using a TPV material – such as other strain-relaxed InGaAs as well as InGaAsSb – with lower band gap than the 0.6 eV material used in the analysis thus far. The metrics of the emitter-TPV cell system using these four different TPV materials can be seen in Table 1. We also evaluated the system at 1500 K to illustrate the potential benefits of higher temperature operation. For each emitter

at both temperatures, the measured emission spectra for each of the 25 arrays was input into our model to maximize the efficiency-power product. The quaternary, 0.52 eV InGaAsSb material outperforms the other three materials at both temperatures due to its low band gap and high EQE peak (>95%).[3] Because we did not design our emitter to overlap with the EQEs of these materials, it is possible that the optimal efficiencies and output powers are higher than what is reported in this table.

TABLE I. Comparison of TPV system metrics with different PV materials. Values were found by maximizing $\eta_{spec}P_{out}$.

TPV Material	Band Gap (eV)	1300 K η_{TPV}	1300 K η_{spec}	1300 K P_{out} (W/cm^2)	1500 K η_{TPV}	1500 K η_{spec}	1500 K P_{out} (W/cm^2)
InGaAs	0.60[24]	0.22	0.43	1.2	0.26	0.52	3.0
	0.55[25]	0.21	0.53	1.2	0.25	0.62	3.2
	0.50[26]	0.17	0.67	1.0	0.20	0.74	2.6
InGaAsSb	0.52[27]	0.24	0.61	1.5	0.27	0.66	3.7

In conclusion, we have demonstrated a spectrally-selective emitter based on a CTE-matched cross-over-a-backplane metasurface which can survive temperature cycling at 1300 K due to the inclusion of an encapsulation layer. Fabricated emitters are predicted to demonstrate η_{TPV} = 0.22, η_{spec} = 0.43, and P_{out} = 1.2 W/cm^2 when coupled to an ideal 0.6 eV InGaAs TPV cell at 1300 K. Further experiments are underway to test longevity as a function of number of thermal cycles, time at elevated temperature, and ambient environmental conditions. Our results indicate that Al_2O_3 encapsulation layer is critical to stabilizing the cross-on-a-backplane geometry when raised to 1300 K. Our design, because of its geometry and heterogeneous structure, can easily be scaled using nanoimprint or stepper lithography in order to cover large surfaces in a cost-effective manner, making it a viable candidate for future commercial TPV systems.

This material is based upon work supported by the Office of Naval Research (ONR) under Contract No. N00014-13-P-1190. Any opinions, findings, and conclusions or recommendations expressed in this material are those of the authors and do not necessarily reflect the views of the ONR. This work was performed, in part, at the Center for Integrated Nanotechnologies (CINT), an Office of Science User Facility operated for the U.S. Department of Energy (DOE) Office of Science. Sandia is a multiprogram laboratory operated by Sandia Corporation, a Lockheed Martin Company, for the United States Department of Energy's National Nuclear Security Administration under Contract DE-AC04-94AL85000.

References:

1. P. Aigrain, The thermophotovoltaic converter. Lecture series given at MIT (1960).
2. L.M. Fraas, J. E. Avery, and H. X. Huang, "Thermophotovoltaic furnace–generator for the home using low bandgap GaSb cells," *Semiconductor Science and Technology* 18.5 (2003): S247.
3. W.R. Chan, P. Bermel, R.C. Pilawa-Podgurski, C.H. Marton, K.F. Jensen, J.J. Senkevich, J.D. Joannopoulos, M. Soljacic, and I. Celanovic, "Toward high-energy-density, high-efficiency, and moderate-temperature chip-scale thermophotovoltaics," *Proceedings of the National Academy of Sciences* 110.14 (2013): 5309-5314.
4. T.J. Coutts and James S. Ward. "Thermophotovoltaic and photovoltaic conversion at high-flux densities," *Electron Devices, IEEE Transactions on* 46.10 (1999): 2145-2153.
5. L.D. Woolf, "Optimum efficiency of single and multiple bandgap cells in thermophotovoltaic energy conversion," *Solar Cells* 19.1 (1986): 19-38.
6. R.A. Lowe, D.L. Chubb, S.C. Farmer, and B.S. Good, "Rare-earth garnet selective emitter," *Applied Physics Letters* 64.26 (1994): 3551-3553.
7. I. Celanovic, N. Jovanovic, and J. Kassakian. "Two-dimensional tungsten photonic crystals as selective thermal emitters," *Applied Physics Letters* 92.19 (2008): 193101.
8. Y. Avitzour, Y.A. Urzhumov, and G. Shvets, "Wide-angle infrared absorber based on a negative-index plasmonic metamaterial," *Physical Review B* 79.4 (2009): 045131.
9. Y. Xiang Yeng, W.R. Chan, V. Rinnerbauer, J.D. Joannopoulos, M. Soljačić, and I. Celanovic, "Performance analysis of experimentally viable photonic crystal enhanced thermophotovoltaic systems," *Optics Express* 21.106 (2013): A1035-A1051.
10. H. Sai, Y. Kanamori, and H. Yugami, "High-temperature resistive surface grating for spectral control of thermal radiation," *Applied Physics Letters* 82.11 (2003): 1685-1687.
11. K.A. Arpin, M.D. Losego, A.N. Cloud, H. Ning, J. Mallek, N.P. Sergeant, L. Zhu, Z. Yu, B. Kalanyan, G.N. Parsons, G.S. Girolami, J.R. Abelson, S. Fan, and P.V. Braun, "Three-dimensional self-assembled photonic crystals with high temperature stability for thermal emission modification," *Nature Communications* 4 (2013).
12. X. Liu, T. Tyler, T. Starr, A.F. Starr, N. Jokerst, and W.J. Padilla, "Taming the blackbody with infrared metamaterials as selective thermal emitters," *Physical Review Letters* 107.4 (2011): 045901.

13. C. Wu, B. Neuner III, J. John, A. Milder, B. Zollars, S. Savoy, and G. Shvets, "Metamaterial-based integrated plasmonic absorber/emitter for solar thermo-photovoltaic systems," *Journal of Optics* 14.2 (2012): 024005.
14. C. Shemelya, D. DeMeo, N.P. Latham, X. Wu, C. Bingham, W. Padilla and T.E. Vandervelde, "Stable high temperature metamaterial emitters for thermophotovoltaics applications," *Applied Physics Letters* 104 (2014): 201113
15. S.L. Murray, F.D. Newman, C.S. Murray, D.M. Wilt, M.W. Wanlass, P. Ahrenkiel, R. Messham, and R.R. Siergiej, "MOCVD Growth of Lattice-Matched and Mismatched InGaAs Materials for Thermophotovoltaic Energy Conversion, " *Semicond. Sci. Technology*, 18, (2003), S202; J.G. Cederberg, J.D. Blaich, G.R. Girard, S.R. Lee, D.P. Nelson, and C.S. Murray, "The development of (InGa)As thermophotovoltaic cells on InP using strain-relaxed In(PAs) buffers," *J. Crystal Growth*, 310, (2008), 3453.
16. L.B. Freund and S. Suresh, *Thin Film Materials* (Cambridge University Press, Cambridge, UK, 2006).
17. Q. Feng, et al., "Engineering the dispersion of metamaterial surface for broadband infrared absorption," *Optics Letters* 37.11 (2012), 2133-2135.
18. H.-T. Chen, "Interference theory of metamaterial perfect absorbers." *Optics Express* 20.7 (2012), 7165-7172.
19. Y.X. Yeng, M. Ghebrebrhan, P. Bermel, W.R. Chan, J. D. Joannopoulos, M. Soljačić, & I. Celanovic, "Enabling high-temperature nanophotonics for energy applications" *Proceedings of the National Academy of Sciences*, 109 (2012), 2280-2285.
20. K. Ujihara, "Reflectivity of metals at high temperatures," *Journal of Applied Physics*, 43 (1972), 2376-2383.
21. S. Deemyad and I. F. Silvera. "Temperature dependence of the emissivity of platinum in the IR." *Review of Scientific Instruments* 79 (2008), 086105.
22. P. Bhattacharya. *Semiconductor Optoelectronic Devices* (Prentice Hall, New Jersey, 1997).
23. C. H. Henry, "Limiting efficiencies of ideal single and multiple energy gap terrestrial solar cells," *Journal of Applied Physics* 51 (1980), 4494–4500.
24. J.G. Cederberg, G.R. Girard, S.R. Lee, J.E. Strauch, G.A. Ten Eyck, SAND Report No. SAND2008-6452, October 2008.
25. C.S. Murray, N. Fatemi, M. Stan, B. Wernsman, and R.J. Wehrer, "Growth, Processing and Characterization of 0.55-eV n/p/n Monolithic Interconnected Modules," *Conference Record of the 28th Photovoltaic Specialists Conference* (2000), 1238.

26. S. Wojtczuk, "Comparison of 0.55eV InGaAs single-junction vs. multi-junction TPV technology, in Thermophotovoltaic Generation of Electricity: TPV3," *AIP Conf. Proc*. 401, (1997), 205.
27. M.W. Dashiell, J.F. Beausang, H. Ehsani, G.J. Nichols, D.M. Depoy, L.R. Danielson, P. Talamo, K.D. Rahner, E.J. Brown, S.R. Burger, P.M. Fourspring, W.F. Topper, Jr., P.F. Baldasaro, C.A. Wang, R.K. Huang, M.K. Connors, G.W. Turner, Z.A. Shellenbarger, G. Taylor, J. Li, R. Martinelli, D. Donetski, S. Anikeev, G.L. Belenky, and S. Luryi, "Quaternary InGaAsSb thermophotovoltaic diodes." *Electron Devices, IEEE Transactions on* 53.12 (2006): 2879-2891.